Mitigation of Finite Bandwidth Effects in Time-Division-Multiplexed SQUID Readout of TES Arrays

Malcolm Durkin, Joseph S. Adams, Simon R. Bandler, James A. Chervenak, Edward V. Denison, William B. Doriese, Shannon M. Duff, Fred M. Finkbeiner, Joseph W. Fowler, Johnathon D. Gard, Gene C. Hilton, Ruslan Hummatov, Kent D. Irwin, Young Il Joe, Richard L. Kelley, Caroline A. Kilbourne, Antoine R. Miniussi, Kelsey M. Morgan, Galen C. O'Neil, Christine G. Pappas, Frederick S. Porter, Carl D. Reintsema, David A. Rudman, Kazuhiro Sakai, Stephen J. Smith, Robert W. Stevens, Daniel S. Swetz, Paul Szypryt, Joel N. Ullom, Leila R. Vale, and Nicholas Wakeham

***Abstract*—Time division multiplexing (TDM) is being developed as the readout technology of the X-ray integral field unit (X-IFU), a 3,168-pixel X-ray transition-edge sensor (TES) imaging spectrometer that is part of the European Space Agency's Athena satellite mission. Recent improvements in the low X-ray event count rate performance of TDM have been driven by increases in multiplexer bandwidth and the mitigation of settling transients. These methods and design changes have improved the 32-row multiplexed resolution of a NASA LPA 2.5a array from an initial (2.73 $\pm$ 0.03) eV to (1.97 $\pm$ 0.01) eV resolution at 5.9 keV. We discuss these recent advances in TDM readout, which have been implemented in an 8-column $\times$ 32-row spectrometer that will be deployed at the Lawrence Livermore National Laboratory electron beam ion trap (EBIT) facility, and present a model that will inform the design of future systems.**

Manuscript received November 30, 2020; revised January 16, 2021; accepted February 15, 2021. Date of publication March 11, 2021; date of current version April 2, 2021. This work was supported by NASA SAT program "Providing Enabling & Enhancing Technologies for a Demonstration Model of the Athena X-IFU." *(Corresponding author: M. Durkin.)*

Malcolm Durkin, Edward V. Denison, William B. Doriese, Shannon M. Duff, Joseph W. Fowler, Johnathon D. Gard, Gene C. Hilton, Young Il Joe, Kelsey M. Morgan, Galen C. O'Neil, Christine G. Pappas, Carl D. Reintsema, David A. Rudman, Robert W. Stevens, Daniel S. Swetz, Paul Szypryt, Joel N. Ullom, and Leila R. Vale are with the National Institute of Standards and Technology, Boulder, CO 80305 USA (e-mail: malcolm.durkin@nist.gov; ed.denison@nist.gov; william.doriese@nist.gov; shannon.duff@nist.gov; joe.fowler@nist.gov; johnathon.gard@nist.gov; gene.hilton@nist.gov; youngil.joe@nist.gov; kelsey.morgan@nist.gov; galen.oneil@nist.gov; christine.pappas@nist.gov; carl.reintsema@nist.gov; david.rudman@nist.gov; robert.stevens@nist.gov; daniel.swetz@nist.gov; paul.szypryt@nist.gov; joel.ullom@nist.gov; leila.vale@nist.gov).

Joseph S. Adams, Simon R. Bandler, James A. Chervenak, Fred M. Finkbeiner, Ruslan Hummatov, Richard L. Kelley, Caroline A. Kilbourne, Antoine R. Miniussi, Frederick S. Porter, Kazuhiro Sakai, Stephen J. Smith, and Nicholas Wakeham are with National Aeronautics and Space Administration, Greenbelt, MD 20771 USA (e-mail: joseph.s.adams@nasa.gov; simon.r.bandler@nasa.gov; james.a.chervenak@nasa.gov; fred.m.finkbeiner@nasa.gov; ruslan.hummatov@nasa.gov; richard.l.kelley@nasa.gov; caroline.a.kilbourne@nasa.gov; antoine.r.miniussi@nasa.gov; frederick.s.porter@nasa.gov; kazuhiro.sakai@nasa.gov; stephen.j.smith@nasa.gov; nicholas.a.wakeham@nasa.gov).

Kent D. Irwin is with the Stanford University Department of Physics, Stanford, CA 94305 USA (e-mail: irwin@stanford.edu).

Color versions of one or more figures in this article are available at https://doi.org/10.1109/TASC.2021.3065279.

Digital Object Identifier 10.1109/TASC.2021.3065279

***Index Terms*—Transition-edge sensors, superconducting quantum interference devices, multiplexed readout, Athena, X-IFU.**

I. Introduction

TRANSITION-EDGE sensor (TES) X-ray microcalorimeters provide electronvolt-scale energy resolution [1] and high collection efficiency [2], which motivates their development for terrestrial experiments and future X-ray observatories. The X-ray integral field unit (X-IFU) [3], which is part of the Athena satellite mission, will perform imaging spectroscopy using a 3168 pixel array of TES X-ray microcalorimeters with the stringent requirements of a 12 keV energy range and 2.5 eV resolution below 7 keV. This kilopixel-scale TES array will require multiplexed readout to meet the instrument's mass and power budgets. X-IFU will use time division multiplexing (TDM).

TDM [4] is a highly mature TES-readout technology that is routinely used in 250-pixel scale TES spectrometers in a broad range of experimental applications [5]. Recent demonstrations have shown steadily improving energy resolutions [6], with the most recent result of (2.16 $\pm$ 0.006) eV at 6.9 keV meeting X-IFU requirements including engineering margins [7]. These advances have been driven by increases in TDM bandwidth and the development of techniques to mitigate the malign effects of settling transients. We discuss these advances and present a model for setting bandwidth requirements in TDM.

TDM involves reading out TES currents sequentially in a multiplexing unit, or column. Our TDM architecture [8] is shown in Fig. 1(a). Each TES's current ($I_{\rm TES}$) is read out as an input flux ($\Phi_{\rm in}$) by a corresponding first stage SQUID (SQ1), which is activated by opening a superconducting flux actuated switch (FAS) [9], [10]. SQ1s in a column are activated one at a time, allowing a column's SQ1 current signals to be read out by one amplifier chain, consisting of a SQUID series array transimpedance amplifier (SSAA) [11], a low noise amplifier (LNA), and an analog to digital converter (ADC). Multiplexing factors as high as 40 have been demonstrated while reading out microcalorimeters [6]. This readout can be scaled further by operating many columns in parallel and activating rows of SQ1s with shared FAS control lines. X-IFU is specified to operate in a

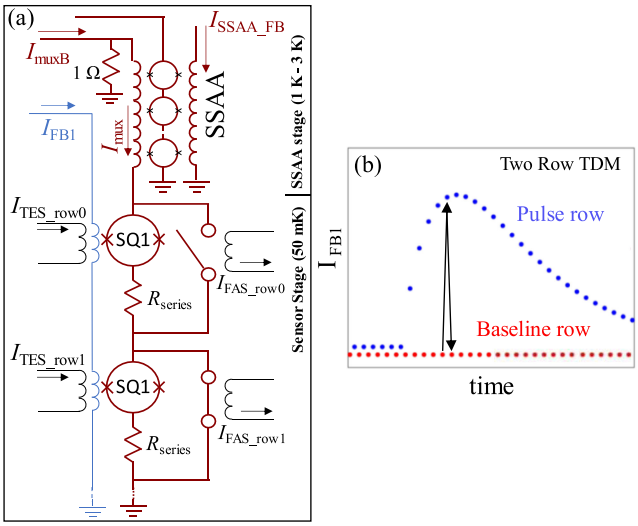

Fig. 1. (a) A circuit diagram of our TDM readout architecture. Each I_{TES} signal is inductively coupled to a SQ1, which is activated by opening a corresponding superconducting flux actuated switch (FAS). The multiplexer output current, I_{mux}, is then read out by an amplifier chain that includes an SSAA. SQ1s are operated in a DFLL, which applies flux feedback via a shared feedback line (FB1) to the active SQ1. (b) A depiction of feedback current during two row TDM readout. When TDM readout switches between rows, the change in I_{FB1} is proportional to the difference in I_{TES} between the two rows.

96-column × 34-row configuration [12], with 33 TESs and one dark row per column.

To linearize the SQUID readout, multiplexed SQ1s are operated in a digital flux locked loop (DFLL) [13], where a feedback current (I_{FB1}) is used to apply flux feedback (Φ_{FB1}) to the active SQ1 so that it has a fixed total applied flux (Φ_{A}). A SQ1's flux lock is maintained with a proportional-integral (PI) controller that measures the SSAA output voltage as an error signal and applies adjustments to I_{FB1} when the SQ1 is activated again during the next readout cycle. As a result of this DFLL, an I_{TES} pulse caused by an X-ray event will have a proportional multiplexed I_{FB1} pulse when its corresponding SQ1 is read out.

To prevent signal degradation, the TDM readout chain must have sufficient bandwidth to switch between SQ1s that are reading out a *baseline* value (no pulse) of I_{TES} and one that is reading out an I_{TES} pulse. A central challenge is that I_{FB1} must change when switching between rows to maintain the DFLL, as shown in Fig. 1(b), a depiction of two-row TDM where one row receives an X-ray pulse. TDM is typically designed to maximize the mutual inductance between the TES coil and SQ1 (M_{in}) while still allowing the highest energy pulse of interest to be tracked [14]. Thus, the change in Φ_{FB1} between baseline in one pixel and a pulse's peak current in the next can correspond to several flux quanta (Φ_0), with a 6 keV pulse having an amplitude of roughly $2\Phi_0$ in the parameter space under discussion for X-IFU.

In this paper, we present measurements and simulations of distortions in SQ1 I_{mux}-Φ curves due to I_{FB1} changes from the previous row, discussing the consequences for readout performance and advances in chip design to mitigate these effects. Since, for fixed bandwidth, these effects worsen as the row-activation duration (t_{row}) is decreased, we focus on the $t_{\mathrm{row}} =$ 160 ns that is specified for X-IFU, which is further divided into a 128 ns delay and a 32 ns sampling time.

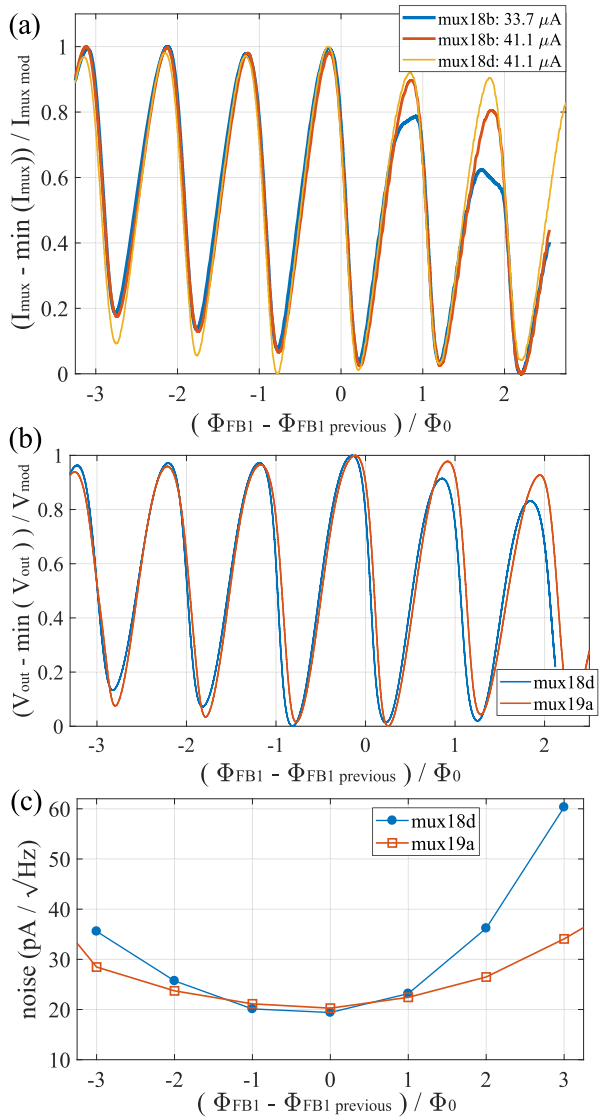

Fig. 2. Settling time effects in TDM with three multiplexer design iterations: mux18b ($I_{\mathrm{cSQ1}} = 10.1$ μA, $M_{\mathrm{FB1}} = 28.9$ pH, $R_{\mathrm{series}} = 1.38$ Ω, $R_{\mathrm{NSQ1}} = 5.37$ Ω), mux18d ($I_{\mathrm{cSQ1}} = 10.2$ μA, $M_{\mathrm{FB1}} = 54.0$ pH, $R_{\mathrm{series}} = 1.48$ Ω, $R_{\mathrm{NSQ1}} = 5.76$ Ω), and mux19a ($I_{\mathrm{cSQ1}} = 12.0$ μA, $M_{\mathrm{FB1}} = 74.5$ pH, $R_{\mathrm{series}} = 2.20$ Ω, $R_{\mathrm{NSQ1}} = 8.56$ Ω). (a) A measurement of the I_{mux} - $\Delta\Phi_{\mathrm{FB1}}$ curve compression of mux18b for two values of I_{muxB}., obtained by flux locking the SSAA. A mux18d measurement is included for comparison. $I_{\mathrm{mux\cdot mod}}$ is the total modulation depth of I_{mux}. (b) The compression of the $\Delta\Phi_{\mathrm{FB1}}$ - V_{SSAA} readout curves, where the SSAA has fixed $I_{\mathrm{SSAA\cdot FB}}$ as it would in TDM readout. Mux19a exhibits less compression than mux18d. (c) The measured readout noise of 40-row TDM as a function of the change in flux from the previous row. Noise is given as an amplitude spectral density referred to the TES current. In (b) and (c), mux18d and mux19a are operated with $I_{\mathrm{muxB}} =$ 39.3 μA and $I_{\mathrm{muxB}} = 72.9$ μA, respectively.

II. Advances in TDM Operation and Chip Design

Experimental measurements were performed in a NIST 8-column × 32-row TDM system and used the NASA LPA 2.5a TES array [15] from our previous work [6], [7]. Our previous work used a "mux18b" multiplexing chip, with parameters listed in the caption of Fig. 2. Distortions in SQUID readout can be quickly visualized by sweeping the Φ_{FB1} applied to one row while keeping the Φ_{FB1} applied to the previous row fixed, as shown in Fig. 2(a). The SQUID curves, whose amplitudes are

constant in the absence of settling effects, visibly compress as the magnitude of the change in Φ_{FB1} between rows increases. The asymmetry in the compression is due to parasitic coupling between the cryostat's FB1 and SQ1 lines, which are adjacent on the twisted pair loom connecting the SSAA stage to the 50 mK stage. This FB1-to-SQ1 line coupling shifts the voltage bias applied to the multiplexer circuit, with the total voltage bias decreasing for positive Φ_{FB1} changes and increasing for negative Φ_{FB1} changes. The multiplexer bias current (I_{muxB}) determines the voltage bias of the multiplexer chip. If I_{muxB} is too low, flat segments where SQ1 voltage bias is zero appear on the curve as in Fig 2(a) when $I_{\mathrm{muxB}} = 33.7\ \mu$A.

Two readout configurations were tested with mux18b at a DFLL lock point 30% of the voltage modulation depth away from an extremum. Config1 was locked near the low I_{mux} side of the SQ1 curve with X-ray pulses going toward positive $\Delta\Phi_{\mathrm{FB1}}$. Config2 was locked near the high side of I_{mux} with X-ray pulses going toward negative $\Delta\Phi_{\mathrm{FB1}}$. The change from the previously default Config1 to Config2 involved reversing the polarity of the TES circuit's current bias, which required physical changes to wire bonds since our architecture is single ended and our room temperature electronics are unipolar.

We measured X-ray spectra of a fluoresced, high-purity Mn source with 1-column $\times$ 32-row multiplexed TESs and fit the obtained spectra to determine the energy resolution of the spectrometer. We found that Config1's resolution rapidly degraded with decreasing t_{row}, with resolutions of (2.73 $\pm$ 0.03) eV FWHM for $t_{\mathrm{row}} = 240$ ns and (2.90 $\pm$ 0.03) eV for $t_{\mathrm{row}} = 200$ ns. In contrast, Config2's resolution improved with decreasing t_{row} due to the reduction in aliased readout noise, with resolutions of (2.53 $\pm$ 0.04) eV for $t_{\mathrm{row}} = 200$ ns and (2.34 $\pm$ 0.04) eV for $t_{\mathrm{row}} = 160$ ns, indicating that the less pronounced compression in the negative $\Delta\Phi_{\mathrm{FB1}}$ direction and the greater dynamic resistance of the higher I_{mux} lock point benefit performance. We were unable to test $t_{\mathrm{row}} < 160$ ns, as this is the shortest t_{row} allowed by our existing TDM digital readout electronics. Our previous reported result, with a resolution of (2.23 $\pm$ 0.02) eV in 40 row-like TDM [6], used Config2.

One limitation of Config2, visible in the mux18b curve in Fig. 2(a), is that positive $\Delta\Phi_{\mathrm{FB1}}$ compression can cause the next row's lock point to be unreachable, causing it to unlock and jump integer Φ_0s towards the pulse peak. In severe cases, chain unlocking can occur, where row unlocks can cause unlocks in other rows. These unlocking events can be avoided by moving the lock point towards the center of the SQUID curves, but this reduces the measurable X-ray event energy range, motivating settling improvements on the positive $\Delta\Phi_{\mathrm{FB1}}$ side as well.

We modified our multiplexer chip designs to improve settling behavior. Increasing SQ1 feedback mutual inductance (M_{FB1}) decreases the I_{FB1} needed for a given Φ_{FB1}. Assuming the parasitic mutual inductance between the FB1 and MUX lines is constant, the voltage induced in the I_{mux} (readout) line by changes in I_{FB1} during pulse readout scales as $1/M_{\mathrm{FB1}}$. Mux18d's M_{FB1} coupling is 1.82 times that of mux18b and mux19a's M_{FB1} coupling is 1.38 times that of mux18d. Additionally, the junction-shunt and series resistances of mux19a are 1.59 times those of mux18d, resulting in a higher dynamic resistance ($R_{\mathrm{dyn}} = \mathrm{d}V/\mathrm{d}I$) and a higher optimal voltage bias. Since X-IFU's 50 mK multiplexer power allocation has been increased to 720 pW per column, the increase in mux19a's operating power remains compliant with instrument budgets.

A comparison between the I_{mux} vs Φ_{FB1} curves of mux18b and mux18d is included in Fig. 2(a). The combined SQUID readout curves for mux18d and mux19a, with I_{muxB} optimized for TDM readout and a fixed value of the flux bias applied to the series array ($I_{\mathrm{SSAA\cdot FB}}$), are shown in Fig. 2(b). The increases to M_{FB1} and R_{dyn} in mux19a reduce compression on both sides of the SQ1 curve. The measured noise of mux18d and mux19a after a change in Φ_{FB1} from the previous rows is shown in Fig. 2(c), with mux19a showing superior performance at large flux changes. This improvement to noise at the peaks of pulses has allowed an 8-column $\times$ 32-row system using mux19a to measure an energy resolution of (1.97 $\pm$ 0.01) eV in the Mn Kα spectrum [7].

III. TDM Circuit Model

We developed TDM circuit simulations to better understand bandwidth dependencies and to set parameters on future chips. An input and output signal diagram of this model is shown in Fig. 3(a). The FB1 and FAS switch control lines have first-order Butterworth low-pass filters. Since the SSAA uses only one roughly linear slope of its V-Φ curve, it is treated as a constant transresistance with a first-order Butterworth filter applied. An anti-aliasing (AA) filter after the LNA is also implemented as a first order Butterworth filter (similar to those used in existing NIST TDM systems.

The multiplexer circuit is simulated by using Kirchoff's rules to obtain a set of differential equations for the circuit in Fig. 1(a), which are solved numerically using a Runge-Kutta method. SQ1 consists of several nominally identical SQUIDs in series. For computational efficiency, SQ1 is implemented as an I_{SQ1}-Φ_{A}-V_{SQ1} lookup table, where SQ1 voltages (V_{SQ1}) are obtained using 2D linear interpolation between table values based on Φ_{A} and SQ1 current (I_{SQ1}). The table itself is obtained by solving SQUID equations via numerical integration [17]. The FAS is a bank of Zappe SQUIDs (Z-SQUIDs) [9] in series, with each Z-SQUID using 4 Josephson junctions of equal area. The Z-SQUIDs have a very low self-inductance parameter ($\beta_{\mathrm{Lsw}} = I_{\mathrm{cFASJJ}}\, L_{\mathrm{switch}} / \Phi_0 << 1$) and a critical current given by

$$I_{\mathrm{csw}} = 2I_{\mathrm{cswJJ}} \left(\cos\left(\pi\Phi_{\mathrm{sw}}/\Phi_0\right) + 1\right) \tag{1}$$

where I_{cswJJ} is the critical current of a Josephson junction in a Z-SQUID, L_{sw} is the inductance of a Z-SQUID, and Φ_{sw} is the total flux applied to each Z-SQUID. In the $\beta_{\mathrm{Lsw}} << 1$ limit and at fixed Φ_{sw}, the Z-SQUIDs have a similar potential-well structure to that of a single junction and thus exhibit single-junction-like dynamic behavior [18]. The low-temperature I_{FAS} -V_{FAS} relation is thus given by

$$V_{\mathrm{FAS}} = R_{\mathrm{NFAS}} \sqrt{\left({I_{\mathrm{FAS}}}^2 - {I_{\mathrm{csw}}}^2\right)} \ \left(I_{\mathrm{FAS}} > I_{\mathrm{csw}}\right) \tag{2}$$

where V_{FAS} is the voltage across the FAS, R_{NFAS} is the normal resistance of the FAS, and I_{FAS} is the current through the FAS. The Z-SQUIDs in an FAS are assumed to be identical and R_{NFAS} is much larger than the SQ1 normal resistance (R_{NSQ1}). This low-temperature-limit approximation is valid because I_{csw} is set and the multiplexer is operated so that $I_{\mathrm{FAS}} >> I_{\mathrm{csw}}$ when the switch is open and $V_{\mathrm{FAS}} = 0$ when the switch is closed, which avoids the strongly temperature-dependent $I_{\mathrm{FAS}} \sim I_{\mathrm{csw}}$ regime.

In absence of settling transients, the simulated multiplexer I_{mux}-Φ_{FB1} curves closely match those measured in experimental systems in shape, modulation depth, and power. A comparison with our mux19a chip is shown in Fig. 3(b).

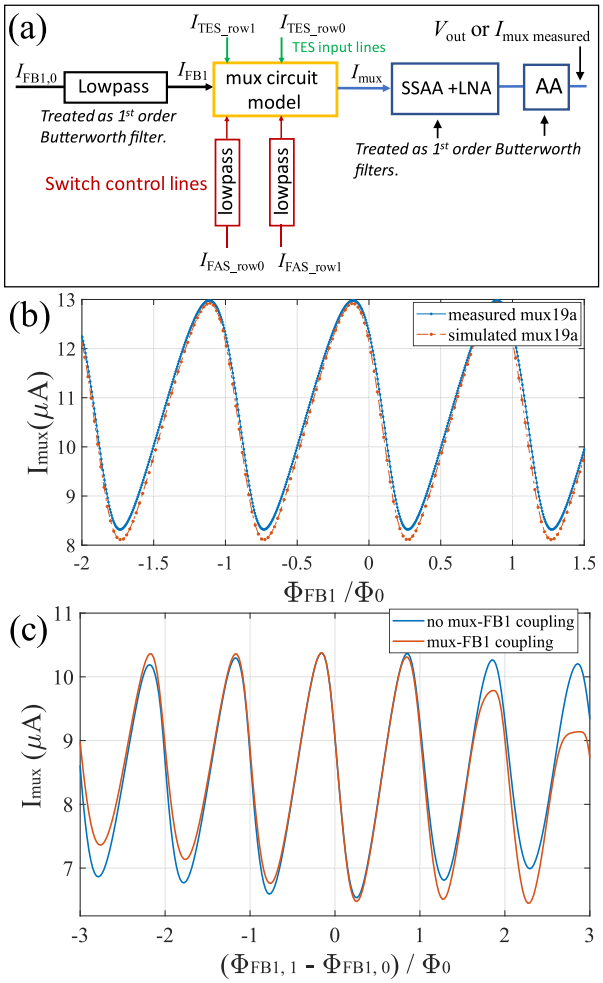

Fig. 3. (a) A signal diagram of TDM readout. Low-pass filters are applied on the FB1 and FAS lines before these signals are applied to the multiplexer model. The output of this model is then sent to the SSAA and the LNA, which are together treated as a low-pass filter. An additional anti-aliasing filter (AA) is applied. (b) A comparison between measured and simulated I_{mux} for a mux19a row, with row activations sufficiently long to make finite bandwidth effects negligible. The mux19a measurement was performed in a 4 K dip probe station used to test multiplexer chips [16], with $I_{muxB} = 68.3\ \mu$A. The simulated curve uses the average parameters measured for the chip described in Fig. 2 and $I_{muxB} = 68.3\ \mu$A, leaving no free parameters. (c) Simulated SQUID curve compression due to finite bandwidths, with and without inductive coupling between mux and FB1 lines. Mux18b chip parameters are used, with coupling and bandwidth parameters chosen to visibly show compression.

The model replicates the distortion in the SQUID curve from settling transients, with distortion shown with and without FB1-SQ1 coupling in Fig. 3(c). Since $R_{NFAS} >> R_{NSQ1}$, the time constant of the circuit is

$$\tau_{mux} = \frac{(L_{SSAA} + L_{interstage} + L_{series})}{(R_{dynSQ1} + R_{series} + R_{interstage} + R_1)} \quad (3)$$

where L_{SSAA} is the self-inductance of the SSAA input coil, $L_{interstage}$ and $R_{interstage}$ are the inductance and resistance of the wiring between the multiplexer and SSAA respectively, R_{series} and L_{series} are the resistances and inductances in series with each SQ1 within a switch loop, and R_{dynSQ1} is the dynamic resistance of SQ1 at settling point. An additional complication in this architecture is a time interval where $V_{SQ1} = 0$ and R_{dynSQ1}

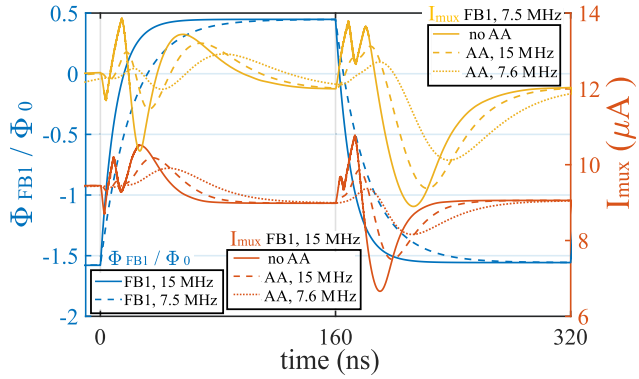

Fig. 4. Simulated switching transients during two row TDM, with varying FB1 and AA cutoffs. $\tau_{mux} \sim 3$ ns was chosen to make effects of AA filter more visible. I_{mux} plots are offset for better visibility. $\Delta\Phi_{FB1} = 2\ \Phi_0$.

$= 0$ when I_{mux} is increasing, resulting in the current rising as

$$\frac{dI_{mux}}{dt} = \frac{R_1\ I_{muxB} - (R_1 + R_{series} + R_{lines})\ I_{mux}}{L_{SSAA} + L_{interstage} + L_{series}} \quad (4)$$

until V_{SQ1} is nonzero and R_{dynSQ1} allows for short τ_{SQ1}. A high rising dI_{mux}/dt is desirable in order to leave the zero V_{SQ1} regime in as little time as possible, but higher $R_1\ I_{muxB}$ results in an increased voltage bias and greater 50 mK power output. This tradeoff between 50 mK power and settling behavior favors low R_{series}, low R_1, and high R_{NSQ1}. However, lower R_1 requires higher I_{muxB} for constant $R_1\ I_{muxB}$, resulting in greater power dissipation on the SSAA stage. These concepts have been incorporated in our 'mux20a' design, which our model and preliminary measurements suggest has roughly half the power output of a mux19a of equivalent bandwidth and modulation depth.

TDM readout performance is not solely determined by multiplexer circuit bandwidth, but also by the other frequency cutoffs in Fig. 3(a). These include a pre-SQ1 modulation cutoff on the FB1 line and several post-modulation cutoffs: the multiplexer circuit, the SSAA, and the anti-aliasing filter (AA). The effects of both types of cutoffs are shown in Fig 4, with settling performance that is more sensitive to pre-modulation than post-modulation cutoffs.

In existing TDM systems, which are single ended, an approximately 10 MHz cutoff is applied to the FB1 line to reduce crosstalk caused by switching between rows. Better isolated cryogenic wiring or the implementation of a differential readout architecture could allow higher frequency cutoffs on the FB1 line, allowing further improvements to TDM bandwidth.

IV. Conclusion

We described advances in multiplexer chip design and operation that increased the analog bandwidth of TDM readout and reduced the effects of settling transients. These changes have driven recent energy-resolution improvements in TDM readout demonstrations [6], [7], allowing readout performance compliant with X-IFU instrument requirements. To aid in setting requirements for future TDM readout systems and in designing multiplexer chips, we developed a numerical model for our readout architecture. This model has been used to optimize the bandwidth-power tradeoff in the mux20a chip, which will be incorporated into the 4-column $\times$ 34 column TDM chip being developed for X-IFU.

REFERENCES

[1] J. Uhlig *et al.*, "High-resolution X-ray emission spectroscopy with transition-edge sensors: Present performance and future potential," *J. Synchrotron Radiat.*, vol. 22, no. 3, pp. 766–775, May 2015.

[2] S. R. Bandler *et al.*, "Advances in small pixel TES-based X-Ray microcalorimeter arrays for solar physics and astrophysics," *IEEE Trans. Appl. Supercond.,* vol. 23, no. 3, Jun. 2013, Art. no. 2100705.

[3] D. Barrett *et al.* "The Athena X-ray integral unit (X-IFU)," *Proc. SPIE*, vol. 9905, Aug. 2016, Art. no. 99052F.

[4] P. A. J. de Korte *et al.*, "Time-division superconducting quantum interference multiplexer for transition-edge sensors," *Rev. Sci. Instrum.*, vol. 74, no. 8, pp. 3807–3815, Aug. 2003.

[5] W. B. Doriese *et al.*, "A practical superconducting-microcalorimeter X-ray spectrometer for beamline and laboratory science," *Rev. Sci. Instrum.,* vol. 88, no. 5, pp. 053108–1-053108-23, Apr. 2017.

[6] M. Durkin *et al.*, "Demonstration of Athena X-IFU compatible 40-row time-division multiplexed readout," *IEEE Trans. Appl. Supercond.,* vol. 29, no. 5, Aug. 2019, Art. no. 2101005.

[7] S. J. Smith *et al.*. "Performance of a broad-band, high resolution, transition-edge spectrometer," *IEEE Trans. Appl. Supercond.*, vol. 31, no. 5, Aug. 2021, Art. no. 2100806.

[8] W. B. Doriese *et al.*, "Developments in time-division multiplexing of X-ray transition-edge sensors," *J. Low Temp. Phys.*, vol. 184, no. 1/2, pp. 389–395, Jul. 2016.

[9] H. H. Zappe, "Josephson quantum interference computer devices," *IEEE Trans. Magn.*, vol. 13, no. 1, pp. 41–42, Jan. 1977.

[10] J. Beyer and D. Drung, "A SQUID multiplexer with superconducting-to-normalconducting switches," *Supercond. Sci Technol.*, vol. 21, no. 10, Oct. 2008, Art. no. 105022.

[11] R. P. Welty and J. M. Martinis, "Two-stage integrated SQUID amplifier with series array output," *IEEE Trans Appl. Supercond.*, vol. 3, no. 1, pp. 2605–2608, Mar. 1993.

[12] H. Geoffray *et al.* "Conceptual design of the detection chain for the X-IFU on Athena," *Proc. SPIE*, vol. 11444, Dec. 2020, Art. no. 114440X.

[13] C. D. Reintsema *et al.*, "Prototype system for superconducting quantum interference device multiplexing of large-format transition-edge sensor arrays," *Rev. Sci. Instrum.,* vol. 74, no. 10, pp. 4500–4508, Oct. 2003.

[14] W. B. Doriese *et al.*, "Optimization of the TES-Bias Circuit for a Multiplexed Microcalorimeter Array," *J. Low Temp. Phys.*, vol. 167, pp. 595–601, Jan. 2012.

[15] A. Miniussi *et al.*, "Performance of an X-ray microcalorimeter with a 240 μm absorber and a 50 μm TES Bilayer," *J. Low Temp. Phys.*, vol. 193, no. 3/4, pp. 337–343, Nov. 2018.

[16] C. D. Reintsema *et al.*, "High-throughput, DC-parametric evaluation of flux-activated-switch based TDM and CDM SQUID multiplexers," *IEEE Trans. Appl. Supercond.,* vol. 29, no. 5, Aug. 2019, Art. no. 2500406.

[17] C. D. Tesche and J. Clarke, "dc SQUID: Noise and optimization," *J. Low Temp. Phys.*, vol. 29, no. 3/4, pp. 301–331, Nov. 1977.

[18] V. Ambegaokar and B. I. Halperin, "Voltage due to thermal noise in the dc Josephson effect," *Phys. Rev. Lett.*, vol. 22, no. 25, pp. 1364–1366, Apr. 1969.